Substrate-Integrated Defected Ground Structure for Single- and Dual-Band Bandpass Filters With Wide Stopband and Low Radiation Loss

Deshan Tang, *Student Member, IEEE*, Changxuan Han, *Student Member, IEEE*, Zhixian Deng, *Graduate Student Member, IEEE*, Huizhen Jenny Qian, *Member, IEEE*, and Xun Luo, *Senior Member, IEEE*

***Abstract*— In this article, two types of substrate-integrated defected ground structure (SIDGS) resonant cells with wide upper stopband and low radiation loss are presented for filter implementation. Such SIDGS resonant cells are composed of two dissimilar DGSs surrounded by the bottom ground and metal-vias, which cannot only introduce wide stopband with low radiation loss but also be flexible for integration. Based on the aforementioned SIDGS resonant cells, single- and dual-band bandpass filters (BPFs) are designed and fabricated. The single-band BPF centered at 2.40 GHz exhibits an ultrawide upper stopband up to 19.7 GHz with a rejection level of 31 dB, whereas the measured stopband total loss (i.e., including radiation, metal, and substrate loss) remains about 30% up to 19.3 GHz. The dual-band BPF operated at 2.10 and 3.78 GHz exhibits an ultrawide upper stopband up to 17.8 GHz with a rejection level of 23 dB, whereas the measured stopband total loss is less than 16% up to 11.4 GHz.**

***Index Terms*— Bandpass filter (BPF), dual-band filter, low radiation loss, single-band filter, slow wave, substrate-integrated defected ground structure (SIDGS), wide stopband.**

I. Introduction

With the increasing development of modern wireless systems, electromagnetic interference (EMI) and interference suppression become major challenges for circuit designs [1]. As a crucial component in such systems, bandpass filters (BPFs) with wide stopband [2] and low radiation loss are urgently demanded. Meanwhile, recent developments of miniaturized multistandard systems [3] require multiband BPF that can be flexibly integrated [4], [5]. Therefore, to satisfy the aforementioned requirements, the BPF should exhibit merits of low radiation loss, wide stopband, multiband operation, and flexibility of integration simultaneously.

Manuscript received July 22, 2020; revised October 18, 2020 and October 26, 2020; accepted October 29, 2020. Date of publication December 1, 2020; date of current version January 5, 2021. This work was supported in part by the National Natural Science Foundation of China under Grant 61934001 and Grant 61904025. This article is an expanded version from the IEEE MTT-S International Microwave Symposium (IMS 2020), Los Angeles, CA, USA, June 21–26, 2020. *(Corresponding author: Xun Luo.)*

The authors are with the Center for Advanced Semiconductor and Integrated Micro-System, University of Electronic Science and Technology of China, Chengdu 611731, China (e-mail: xun-luo@ieee.org).

Color versions of one or more of the figures in this article are available online at https://ieeexplore.ieee.org.

Digital Object Identifier 10.1109/TMTT.2020.3038202

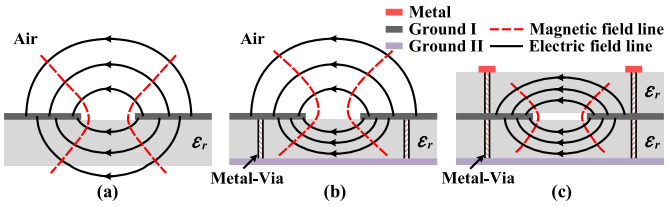

Fig. 1. (a) Field distributions on the DGS. (b) Field distributions on the DGS with ground shield and metal-vias. (c) Field distributions on the SIDGS.

Recently, multiple methods are introduced to implement BPFs with good performance. The single-band [6]–[8] and dual-band [9] substrate-integrated waveguide (SIW) filters are proposed with good in-band performance and low radiation loss. However, the stopband bandwidth of these filters is limited. To extend the stopband bandwidth, the wiggly line [10], compact microstrip resonant cell resonator [11], parallel-coupled line [12], and periodically nonuniform coupled microstrip line [13] are proposed for single-band design, while the CPW-to-microstrip [14] and net-type resonators [15] are proposed for dual-band design. Nevertheless, these structures either suffer from a high insertion loss or a low stopband rejection level. To further extend the stopband bandwidth with enhanced stopband rejection level, single- and dual-band BPFs using stepped-impedance resonators (SIRs) [16]–[22] and defected ground structure (DGS) cells [23]–[25] are proposed. However, the radiation loss at stopband still remains a great challenge. For example, as shown in Fig. 1(a), the EM field of DGS is divergent and affected by adjacent devices, which means that such DGS is not suitable for system integration. Therefore, the flexibly integrated BPFs with wide stopband and low radiation still need to be further investigated.

As shown in Fig. 1(b), the DGS shielded by surrounding metal-vias and bottom ground II could confine most of the EM field between the DGS and bottom ground. Then, to further reduce the radiation loss, the substrate-integrated DGS (SIDGS) is proposed [26], as shown in Fig. 1(c), where the DGS is fully integrated into the substrate. Meanwhile, the metal-vias connected to the upper layer could confine the upward EM field in the substrate. Therefore, the radiation

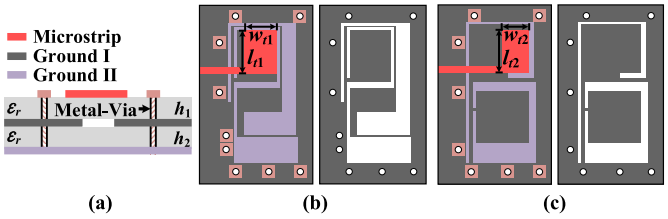

Fig. 2. Configurations of the proposed SIDGS resonant cells. (a) Layer schematic. (b) Type-A SIDGS cell. (c) Type-B SIDGS cell.

loss is suppressed and the proposed SIDGS resonant cells can be integrated into wireless system without suffering from the performance degeneration caused by the influence from nearby circuits. Then, two types of SIDGS resonant cells are proposed for BPF designs. Each SIDGS resonant cell can introduce an ultrawide stopband with high stopband rejection level. Based on such SIDGS cells, two compact BPFs with single- and dual-band operations are designed and fabricated, respectively. The measured results exhibit merits of low radiation loss, wide stopband with high rejection level, and low insertion loss.

In [26], a single-band BPF using SIDGS is designed and fabricated. Following the previous SIDGS BPF design, this article expands the detailed theoretical analysis of SIDGS cells for filter design, including resonance, spurious suppression, and radiation suppression. Meanwhile, a new dual-band BPF using SIDGS is proposed and the related design method is discussed. In Section II, the detailed analysis of the proposed two types of SIDGS resonant cells is presented including resonance, spurious suppression, and radiation suppression. Section III demonstrates the coupled schemes of two types of SIDGS resonant cells. After that, Section IV presents the design examples of single- and dual-band BPFs based on SIDGS resonant cells. Finally, a brief conclusion is given in Section V.

II. Substrate-Integrated Defected Ground Structure

Fig. 1(a) shows the E-field and H-field distributions of a conventional DGS, where the EM field is not constrained, which results in a large radiation loss [27]. Then, to decrease the radiation loss, the surrounding metal-vias and bottom ground II can be utilized and integrated with DGS structures. As shown in Fig. 1(c), the EM field is mostly confined in the substrate, which effectively minimizes the radiation loss. Based on the basic concept of SIDGS mentioned earlier, two types of SIDGS resonant cells (i.e., type-A and type-B) are proposed, as shown in Fig. 2, which are employed for single- and dual-band filter implementations with specific coupling schemes. Both SIDGS resonant cells are composed of two stepped-impedance DGSs, which are surrounded by the bottom ground and metal-vias. To fulfill the coupling scheme for a resonator-coupled filter, the coupling side of the cell could not locate metal-vias. Note that the physical size of these DGSs cannot meet the theoretical definition of slotline [27] (i.e., $W<0.25\lambda_g/\sqrt{\varepsilon_r}$, $W/h\leq 1$, and $b\leq 7W$, where W is the width of the slot, b is the width of the metallization, and

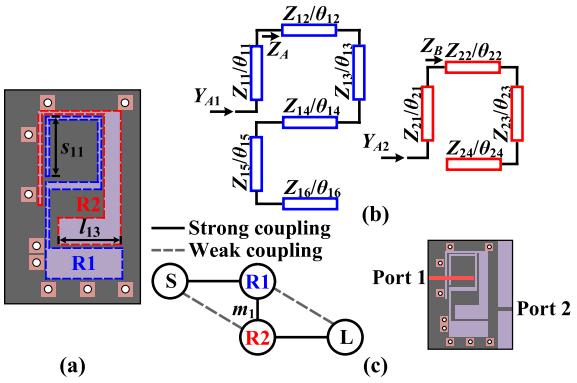

Fig. 3. (a) Configurations of resonators R1 and R2 in type-A SIDGS cell. (b) Simplified equivalent circuits of R1 and R2. (c) Coupling scheme and feeding scheme of R1 and R2.

h is the thickness of the substrate). The stepped-impedance microstrip is introduced as the feed line in each cell. To further investigate the mechanism of proposed SIDGS resonant cells, the dielectric substrate RO4003C (i.e., $\varepsilon_r = 3.55$, $h_1 = 0.203$ mm, and $h_2 = 0.303$ mm) and EM simulator HFSS are used.

A. Resonance

It is known that the etched defect in a DGS disturbs the current distribution on the ground [28], which implies that the DGSs integrated with the surrounding ground and metal-vias in each cell possess their own resonant frequencies.

Fig. 3(a) and (b) shows the configurations and equivalent circuits of two SIDGS resonators (i.e., R1 and R2) in the type-A SIDGS cell. Then, the input admittances of two resonators (i.e., Y_{A1} and Y_{A2}) are derived as follows:

$$Y_{A1} = \frac{Z_{11} + jZ_A \tan\theta_{11}}{Z_{11}(Z_A + jZ_{11}\tan\theta_{11})} \tag{1}$$

$$Y_{A2} = \frac{Z_{21} + jZ_B \tan\theta_{21}}{Z_{21}(Z_B + jZ_{21}\tan\theta_{21})} \tag{2}$$

where Z_A and Z_B are the input impedances defined in Fig. 3(b). The detailed derivations are presented in the Appendix. The resonant frequencies (i.e., f_{11} and f_{12}) of these two separate resonators are obtained under the cases of $Y_{A1} = 0$ and $Y_{A2} = 0$, respectively. Here, the microstrip line source and load ports (i.e., ports 1 and 2) are introduced to extract the resonant characteristics of type-A SIDGS cell, and the coupling scheme of the resonators is shown in Fig. 3(c). The resonant frequencies of the cell f_{p1}, f_{p2} are derived as follows [29]:

$$f_{p1,p2} = \sqrt{\frac{f_{11}^{-2} + f_{12}^{-2} \pm \sqrt{\left(f_{11}^{-2} + f_{12}^{-2}\right)^2 + 4m_1^2 f_{11}^{-2} f_{12}^{-2}}}{2f_{11}^{-2} f_{12}^{-2}\left(1 - m_1^2\right)}} \tag{3}$$

where m_1 is the coupling coefficient of these two resonators obtained by simulation [29] and f_{11} and f_{12} are the resonant frequencies of separated SIDGS resonators. Fig. 4(a) and (b) shows the calculated and simulated resonant frequencies

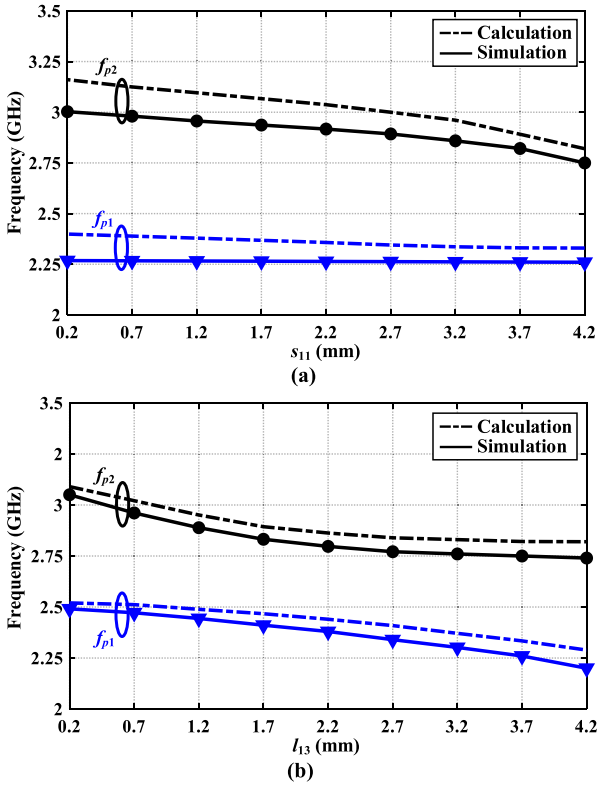

Fig. 4. (a) Effect of s_{11} on the resonant frequencies of the type-A SIDGS cell. (b) Effect of l_{13} on the resonant frequencies of the type-A SIDGS cell.

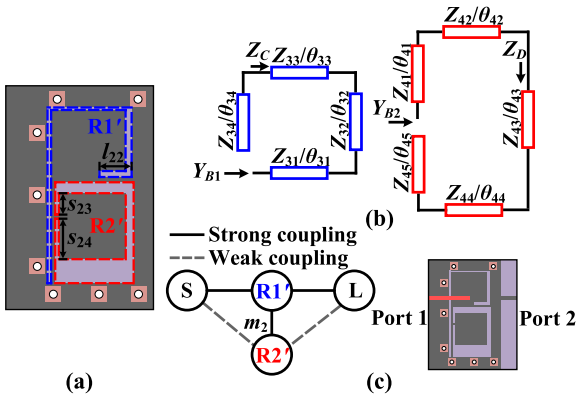

Fig. 5. (a) Configurations of resonators R1′ and R2′ in type-B SIDGS cell. (b) Simplified equivalent circuits of R1′ and R2′. (c) Coupling scheme and feeding scheme of R1′ and R2′.

f_{p1} and f_{p2} with the variation of s_{11} and l_{13}, respectively. The electrical length and characteristic impedance of the SIDGS resonators can be extracted by full-wave simulation. Good agreement between the calculation and the simulation is achieved.

Fig. 5(a) and (b) shows the configurations and equivalent circuits of two SIDGS resonators (i.e., R1′ and R2′) of type-B SIDGS cell. Then, the input admittances of two resonators (i.e., Y_{B1} and Y_{B2}) are derived in (4) and (5) [as shown at the bottom of the page] as follows:

$$Y_{B1} = \frac{Z_{31} + jZ_C \tan\theta_{31}}{Z_{31}(Z_C + jZ_{31}\tan\theta_{31})} \tag{4}$$

where Z_C and Z_D are the input impedances defined in Fig. 4(b). The Appendix presents the detailed derivations. $Y_{B1} = 0$ and $Y_{B2} = 0$ are the resonant conditions for these two separate resonators. To discuss the resonant characteristics of type-B SIDGS cell, the coupling scheme of the resonators is shown in Fig. 5(c). Note that the peninsula topology cannot only generate dual resonance but also introduce a deep transmission zero between two resonances [30], [31]. The resonant frequencies of the whole SIDGS resonant cell at f_{d1} and f_{d2} are defined as [25]

$$f_{d1,d2} = \sqrt{\frac{M_1 \pm \sqrt{M_1^2 - 4M_2^2}}{2}} \tag{6}$$

where M_1 and M_2 are expressed as

$$M_1 = f_{21}^2 + f_{22}^2 + \frac{m_2^2 f_{21} f_{22}}{\gamma_{21}\gamma_{22}} \tag{7}$$

$$M_2 = f_{21}^2 f_{22}^2. \tag{8}$$

Note that f_{21} and f_{22} are the resonant frequencies of the separate SIDGS resonators. γ_{21} and γ_{22} are the parameters that define the transformations of two resonators [30]. m_2 is the coupling coefficient between these two resonators. Fig. 6(a) and (b) shows the calculated and simulated resonant frequencies of type-B SIDGS cell under different dimensions (i.e., l_{22} and $s_m = s_{23} + s_{24}$), respectively. f_{d1} and f_{d2} are decreasing as the increasing of l_{22} and s_m. The results between calculation and simulation agree well.

B. Spurious Suppression

To discuss the harmonic shifting, a simplified capacitively loaded slow-wave transmission line will be discussed first, as shown in Fig. 7(a). By using the ABCD matrix [32], the characteristic equations of the circuit are expressed as follows:

$$2\pi f_0 C_1 - 2\pi f_0 C_2 \cos\theta_{a0} = \frac{1}{Z_a}\sin\theta_{a0} \tag{9}$$

$$2\pi f_1 C_1 + 2\pi f_1 C_2 \cos\theta_{a1} = -\frac{1}{Z_a}\sin\theta_{a1} \tag{10}$$

$$\cos(\beta d) = \cos\theta_a - \frac{1}{2}\omega(C_1 + C_2)Z_a \sin\theta_a \tag{11}$$

where Z_a and θ_a are the characteristic impedance and the electric length of the unloaded transmission line, respectively, f_0 is the fundamental resonant frequency, f_1 is the first spurious resonant frequency, and β is the propagation constant

$$Y_{B2} = \frac{1}{Z_{41}} \cdot \frac{Z_{41}(Z_{42} + jZ_D\tan\theta_{42}) + jZ_{42}\tan\theta_{41}(Z_D + jZ_{42}\tan\theta_{42})}{Z_{42}(Z_D + jZ_{42}\tan\theta_{42}) + jZ_{41}\tan\theta_{41}(Z_{42} + jZ_D\tan\theta_{42})} \tag{5}$$

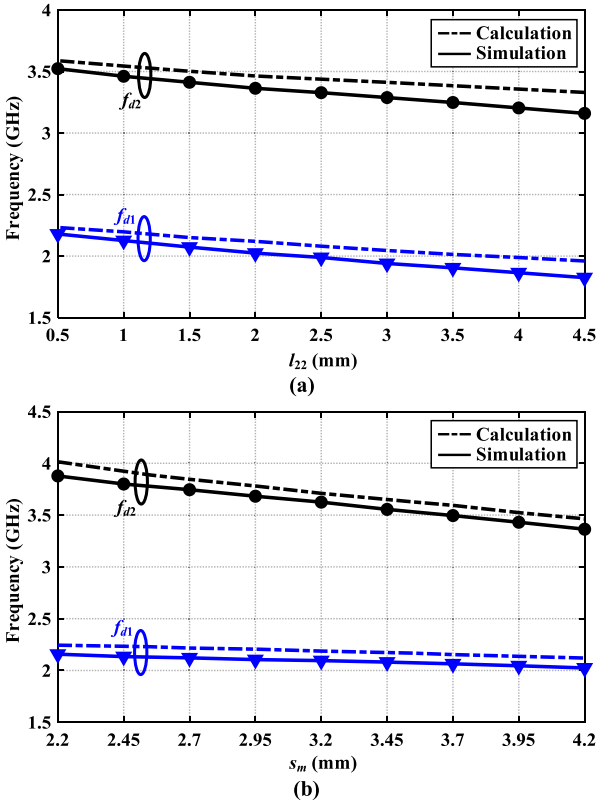

Fig. 6. (a) Effect of l_{22} on the resonant frequencies of the type-B SIDGS cell. (b) Effect of s_m on the resonant frequencies of the type-B SIDGS cell.

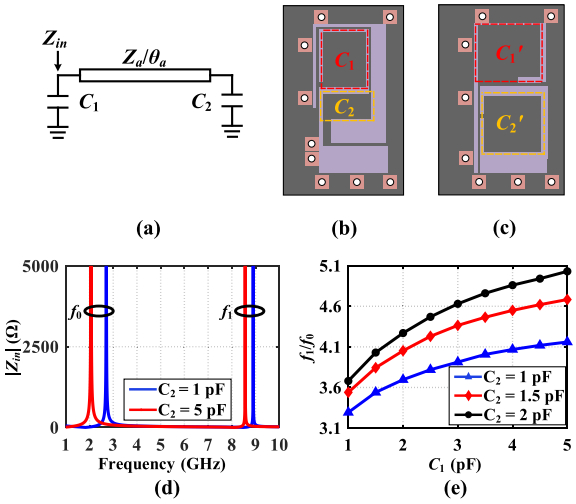

Fig. 7. (a) Simplified capacitively loaded slow-wave circuit. (b) Capacitor distribution of type-A cell. (c) Capacitor distribution of type-B cell. (d) Input impedance of the capacitively loaded slow-wave circuit under the case of $C_1 = 1$ pF. (e) Calculated ratio of the spurious resonant frequency to the fundamental one for different capacitance loading.

of the loaded transmission line. Fig. 7(d) plots the input impedance of the capacitively loaded slow-wave circuit under the case of $C_1 = 1$ pF and an ideal transmission line (100-Ω characteristic impedance and 180° electrical length at 8 GHz). Meanwhile, the calculated ratios of the spurious resonant frequency to the fundamental one for different capacitance loading are presented in Fig. 7(e). It implies that the ratio is increased with the loading capacitance increasing, indicating

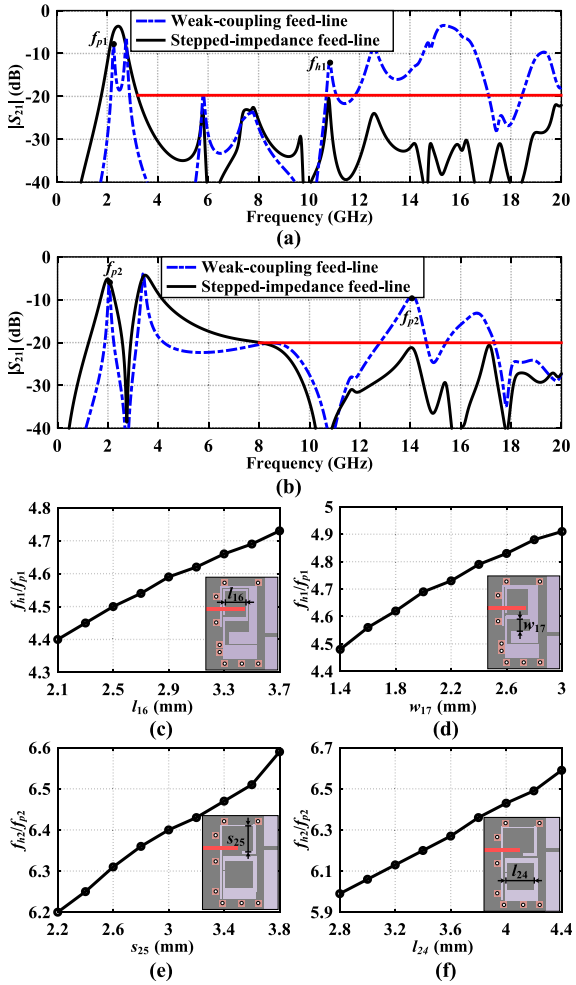

Fig. 8. (a) Simulated frequency responses of the type-A SIDGS cell with weak-coupling feed line and strong-coupling stepped-impedance feed line. (b) Simulated frequency responses of the type-B SIDGS cell with weak-coupling feed line and strong-coupling stepped-impedance feed line. (c) Effect of the dimension l_{16} on f_{h1}/f_{p1}. (d) Effect of the dimension w_{17} on f_{h1}/f_{p1}. (e) Effect of the dimension s_{25} on f_{h2}/f_{p2}. (f) Effect of the dimension l_{24} on f_{h2}/f_{p2}.

the slow-wave effect [32]. Fig. 7(b) and (c) shows the capacitor distribution (i.e., C_1, C_2, C_1', and C_2') [33] of two types of the SIDGS cells. Note that the integrated ground II could further increase the effective capacitance in each capacitor area. Thus, the slow-wave model in Fig. 7(a) is used to explain wide stopband characteristics of the cells. To verify the slow-wave effect, the simulated transmission responses in the weak-coupled feeding scheme are presented in Fig. 8(a) and (b). The ratios of the spurious resonant frequency to the fundamental one f_{h1}/f_{p1} with different capacitors' dimensions in type-A cell are plotted in Fig. 8(c) and (d), whereas the ratios of type-B cell (i.e., f_{h2}/f_{p2}) are plotted in Fig. 8(e) and (f). Note that the wider metal pad with smaller DGS width could generate a larger effective capacitance. Therefore, the increasing of l_{16} and w_{17} means a larger effective capacitance in C_1 and C_2. Then, the value of f_{h1}/f_{p1} is enhanced and a wider stopband performance in the type-A cell is achieved. Meanwhile, the increasing of s_{25} and l_{24} means a larger effective capacitance in C_1' and C_2'. Therefore, the value of

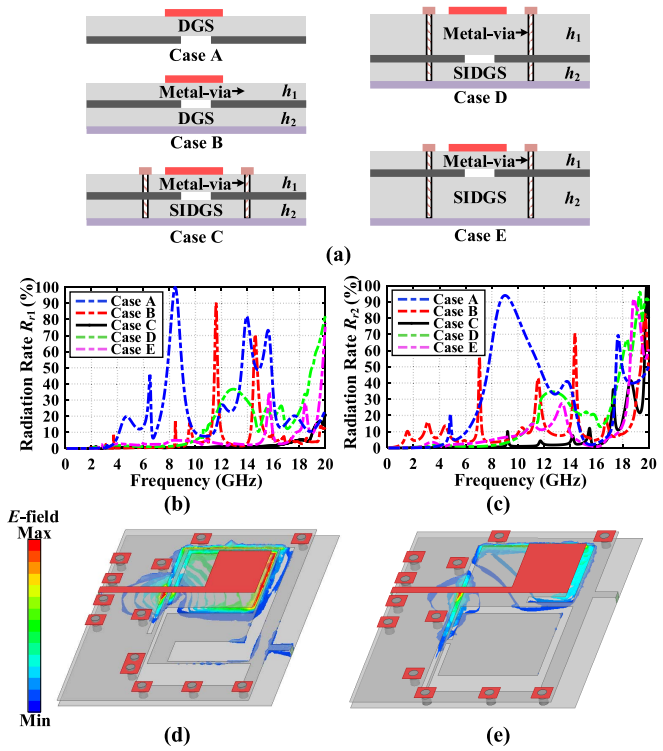

Fig. 9. (a) Configuration of five cases of the cells. (b) Radiation rate R_{r1} of the type-A cell in five cases under the condition of lossless substrate and metal. (c) Radiation rate R_{r2} of the type-B cell in five cases under the condition of lossless substrate and metal. (d) Simulated E-field of the substrate between ground I and ground II at stopband (i.e., 8 GHz) in the type-A SIDGS cell. (e) Simulated E-field of the substrate between grounds I and II at stopband (i.e., 8 GHz) in the type-B SIDGS cell.

f_{h2}/f_{p2} is enhanced and a wider stopband performance in the type-B cell is achieved.

In addition, the stepped-impedance feed line is used in the strong-coupling feeding scheme of two types of the SIDGS cells to enhance the stopband rejection level at higher frequency. The external quality factors of the cells in the strong-coupling feeding scheme are decreased compared with the weak-coupling feeding scheme [29]. Note that too large or too small external quality factor could increase mismatch and reduce the resonant strength of the coupled resonators in filter design [29]. As shown in Fig. 8(a) and (b), the larger external quality factor increases the mismatch at the fundamental resonant frequency in the weak-coupling feeding scheme. Thus, the decreasing of the external quality factor could decrease the mismatch and increase the fundamental resonant strength. Meanwhile, the smaller external quality factor increases the mismatch at the spurious resonant frequency in the weak-coupling feeding scheme. Thus, the decreasing of the external quality factor could further increase the mismatch and decrease the spurious resonant strength. As a result, the spurious suppression at higher frequency is improved by using the strong coupling stepped-impedance feed line.

C. Radiation Suppression

The radiation suppression of the SIDGS cells could be discussed in the following three parts with five cases (i.e., case A–E) shown in Fig. 9(a).

1) Shield Ground II: Compared with the conventional DGS, ground II is an additional boundary condition in the SIDGS. Such a boundary condition can restrict the E-field and H-field between the two conductors, which decreases the radiation loss of the structure. To verify the function of ground II, radiation loss rates (i.e., R_{r1} and R_{r2}) of the type-A and type-B cells without ground II and metal-vias (i.e., case A) and with ground II and without metal-vias (i.e., case B) are simulated under the case of lossless substrate and metal, as shown as the blue and red dashed curves in Fig. 9(b) and (c). R_r is calculated by

$$R_r = 1 - |S_{11}|^2 - |S_{21}|^2. \tag{12}$$

Note that compared with case A, the radiation in case B is decreased by the shield ground II.

2) Surrounding Metal-Vias: Even though the shield ground II is introduced, the conductor-backed DGS will also radiate at high frequency due to the wave leaking from the edge of the two conductors [34]. Then, the metal-vias surrounding the conductor-backed DGS are proposed. Note that the metal-vias guarantee the middle metal layer grounded. Thus, unwanted outward-traveling TEM waves between the middle metal layer and the bottom metal layer in conductor-backed DGS [34] are decreased, which further minimizes the radiation. Meanwhile, two adjacent metal-vias with grounds I and II connected can be regarded as a rectangular waveguide. The cutoff frequency of a rectangular waveguide can be expressed as follows [35]:

$$f_{c10} = \frac{1}{2a\sqrt{\mu\varepsilon}} \tag{13}$$

where a is the distance between two metal-vias. Thus, for $f < f_{c10}$, the E-field and H-field will be blocked, which further reduces the radiation loss of the structure. To verify the function of metal-vias, the radiation loss rates of the type-A and type-B cells with ground II and metal-vias ($h_1 = 0.203$ mm and $h_2 = 0.303$ mm) (i.e., case C) are shown as the black solid curves in Fig. 9(b) and (c). Compared with cases A and B, the radiation in case C is further reduced by the metal-vias.

3) Substrate Thickness of the SIDGS: It is known that a surface wave is a propagating mode guided by the air–dielectric surface for a dielectric substrate on the conductor ground plane [29, p. 82]. With the increase of the substrate thickness, the surface wave is easier to propagate, which will cause high radiation. Considering the fabrication limitation, two relatively thin substrates are chosen to decrease the radiation in the implementation of the SIDGS cells. To verify the effect of the substrate thickness, radiation loss rates of the type-A and type-B cells with ground II and metal-vias ($h_1 = 1$ mm and $h_2 = 0.303$ mm) (i.e., case D) and with ground II and metal-vias ($h_1 = 0.203$ mm and $h_2 = 1$ mm) (i.e., case E) are presented as the green and purple dash curves in Fig. 9(b) and (c). Note that for two tiers of substrates, the thickness of the upper substrate has a greater influence on the radiation since the upper substrate has a larger surface contacted with air, which is easier to propagate the surface wave.

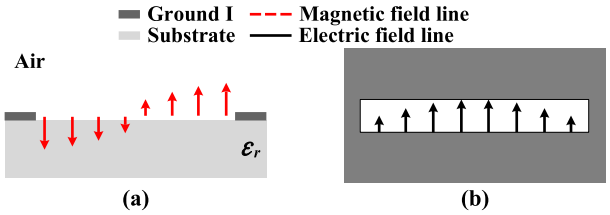

Fig. 10. Field distribution of the DGS line resonator at fundamental resonance. (a) Magnetic field. (b) Electric field.

To investigate the radiation characteristics of SIDGS resonant cells, the EM-simulated E-field of the substrate between grounds I and II in two types of cells under case C at stopband is shown in Fig. 9(d) and (e). Note that the E-field is concentrated near the DGS in the substrate. Most E-field is confined in the substrate by using metal-vias and surrounding ground.

III. SIDGS Resonant Cells With Quasi-Coupled Schemes

Two identical SIDGS resonant cells can be utilized to design a coupled filter, and each SIDGS resonant cell is constituted of two dissimilar SIDGS resonators. First, to illustrate the coupling characteristics of SIDGS, the field distributions of the DGS line resonator at fundamental resonance are shown in Fig. 10. Note that each of the DGS line resonators has the maximum electric field density and the minimal magnetic field density at the middle of the line. Meanwhile, it has the maximum magnetic field density and the minimal electric field density at the end of the line [27]. The field distribution could be verified by simulation. By properly adjusting the physical dimension and the configuration of the coupled SIDGS resonators, the magnetic coupling and electric coupling can be obtained for filter design. Then, the coupling coefficient k_{ij} of the asynchronous SIDGS resonant cells can be extracted by the following equation:

$$k_{ij} = \frac{1}{2}\left(\frac{f_{0i}}{f_{0j}} + \frac{f_{0j}}{f_{0i}}\right)\sqrt{\left(\frac{f_{pi,di}^2 - f_{pj,dj}^2}{f_{pj,dj}^2 + f_{pi,di}^2}\right)^2 - \left(\frac{f_{0i}^2 - f_{0j}^2}{f_{0i}^2 + f_{0j}^2}\right)^2} \tag{14}$$

where f_{0i} and f_{0j} are the resonant frequencies of the dissimilar SIDGS resonators and $f_{pi,di}$ and $f_{pj,dj}$ are the resonant frequencies of two resonators under the coupled conditions in type-A and type-B SIDGS resonant cells, respectively. Here, the two resonant frequencies of these SIDGS resonators are set to be equal, and thus, (14) could be simplified as [29]

$$k_{ij} = \frac{f_{pi,di}^2 - f_{pj,dj}^2}{f_{pj,dj}^2 + f_{pi,di}^2}. \tag{15}$$

Fig. 11 shows the configuration of the coupling scheme and the coupling-node diagram of two type-A SIDGS cells. Then, the couplings of these coupled cells could be concluded in six parts: 1) broadside coupling k_{23} between R2 and R3; 2) embedded couplings between R1 and R2 (i.e., k_{12}) and R3 and R4 (i.e., k_{34}); 3) cross coupling k_{14} between

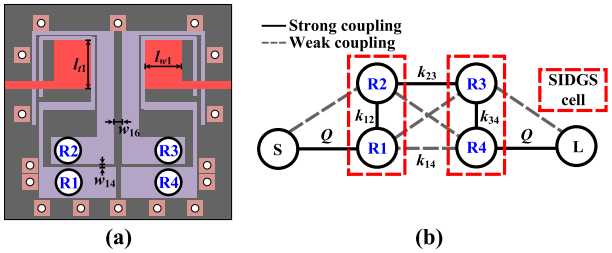

Fig. 11. (a) Configuration of two coupled type-A SIDGS cells. (b) Coupling scheme of two type-A SIDGS resonant cells.

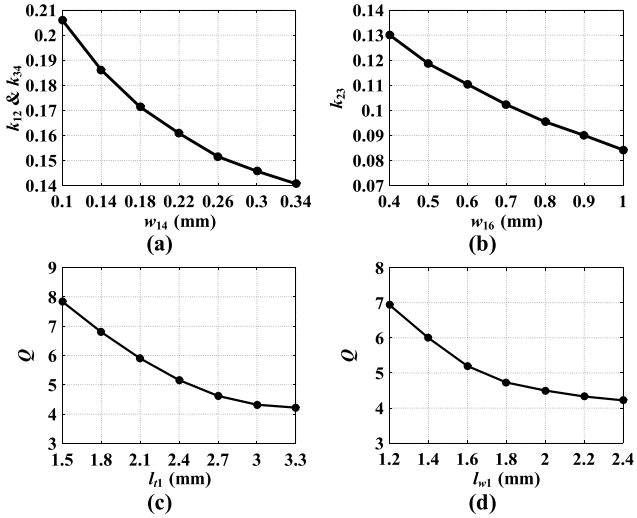

Fig. 12. (a) Effect of the dimension w_{14} on the coupling coefficients k_{12} and k_{34}. (b) Effect of the dimension w_{16} on the coupling coefficient k_{23}. (c) Effect of the dimension l_{t1} on the external quality factor Q. (d) Effect of the dimension l_{w1} on the external quality factor Q.

R1 and R4; 4) coupling k_{S1} and k_{4L} between microstrip feed line and R1 or R4, respectively; 5) tiny couplings between microstrip feed line and R2 or R3; and 6) diagonal couplings including k_{13} and k_{24}. Note that the strong couplings, such as k_{12}, k_{23}, and k_{34}, are mainly generated at the middle of the DGS line resonators, which are dominated by the electric field. The cross coupling of R1 and R4 is mainly produced at the end of the DGS, which is dominated by magnetic field. In this design, the electrical coupling is regarded as positive coupling and the magnetic coupling is regarded as negative coupling. The main couplings k_{12}, k_{34}, and k_{23} are simulated and shown in Fig. 12(a) and (b). The coupling coefficients k_{12}, k_{34}, and k_{23} are increasing with the decreasing widths of the gaps (i.e., w_{14} and w_{16}). Meanwhile, Fig. 12(c) and (d) shows that the external quality factor Q is decreasing with the increase of l_{t1} or l_{w1}.

Fig. 13 shows the configuration of the coupling scheme and the coupling-node diagram of type-B SIDGS cell. Different from the coupling scheme of type-A SIDGS cells, k'_{23} is weak coupling, whereas k'_{14} is strong coupling in the coupling scheme of type-B SIDGS cells. Note that the strong couplings, such as k'_{12}, k'_{14}, and k'_{34}, are mainly generated at the end of the DGS line resonators, which are dominated by the magnetic field. The cross coupling of R2′ and R3′ is mainly produced at

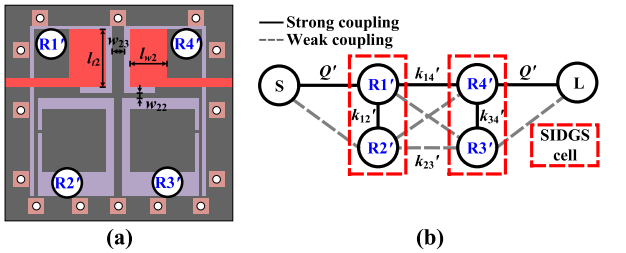

Fig. 13. (a) Configuration of two coupled type-B SIDGS cells. (b) Coupling scheme of two type-B SIDGS resonant cells.

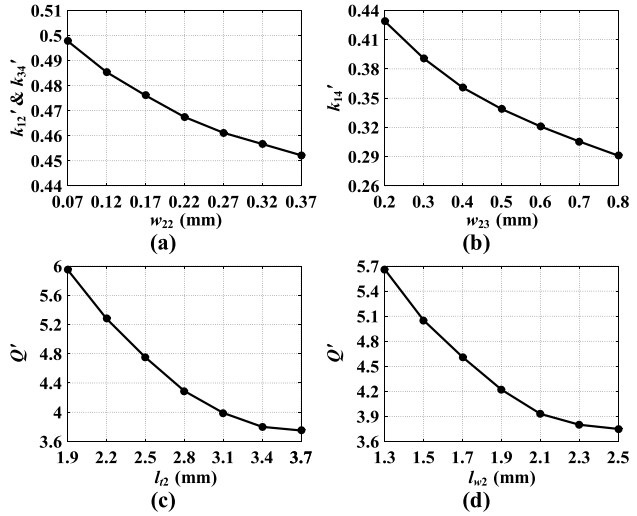

Fig. 14. (a) Effect of the dimension w_{22} on the coupling coefficients k'_{12} and k'_{34}. (b) Effect of the dimension w_{23} on the coupling coefficient k'_{14}. (c) Effect of the dimension l_{t2} on the external quality factor Q'. (d) Effect of the dimension l_{w2} on the external quality factor Q'.

the middle of the DGS, which is dominated by electric field. In this design, the magnetic coupling is regarded as positive coupling and the electric coupling is regarded as negative coupling. The main couplings k'_{12}, k'_{34}, and k'_{14} are simulated and shown in Fig. 14(a) and (b). The coupling coefficients k'_{12}, k'_{34}, and k'_{14} are increasing with the decreasing widths of the gaps (i.e., w_{22} and w_{23}). Meanwhile, Fig. 14(c) and (d) shows that the external quality factor Q' is decreasing with the increasing of l_{t2} or l_{w2}.

IV. Design Example

To verify the aforementioned principle, a single-band BPF and a dual-band BPF with wide upper stopband and low radiation loss are presented and fabricated. The dielectric substrate RO4003C (i.e., $\varepsilon_r = 3.55$, $h_1 = 0.203$ mm, and $h_2 = 0.303$ mm) is utilized for the manufacturing.

A. Single-Band BPF Design

Based on the type-A SIDGS cell, a prototype of a four-order single-band BPF is proposed, as shown in Fig. 15. Two type-A SIDGS cells are coupled using a symmetric coupled scheme. Then, the BPF is implemented with specifications as follows:

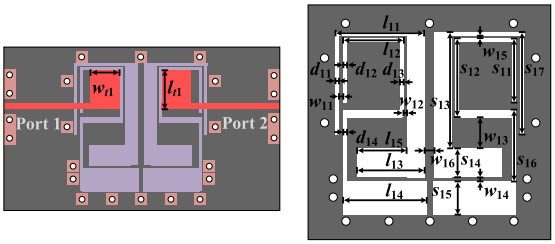

Fig. 15. Configuration of the single-band BPF. (a) Top view. (b) Details of the middle layer.

center frequency of 2.4 GHz, 3-dB FBW = 25.0%, 20-dB return loss, and two transmission zeros at 1.0 and 3.6 GHz close to passband introduced by cross coupling to enhance passband selectivity. The optimized coupling matrix $[M_p]$ can be exhibited as follows [36]:

$$\begin{pmatrix} 0 & 0.9651 & 0.0101 & 0 & 0 & 0 \\ 0.9651 & 0 & 0.6342 & 0.0290 & -0.0135 & 0 \\ 0.0101 & 0.6342 & 0 & 0.4564 & 0.0290 & 0 \\ 0 & 0.0290 & 0.4564 & 0 & 0.6342 & 0.0101 \\ 0 & -0.0135 & 0.0290 & 0.6342 & 0 & 0.9651 \\ 0 & 0 & 0 & 0.0101 & 0.9651 & 0 \end{pmatrix}. \tag{16}$$

Compared with the traditional design using coupling matrix, the fractional bandwidth of 25% is larger. Since the wideband definition in cases [37]–[40] is larger than 40%, 25% is considered as the edge between wideband and narrowband. Thus, the coupling matrix is used as a reference for filter design. To achieve the filter with high agreement with the design specification, the physical dimensions of the filters could be optimized at the later stage. The center frequency is determined by the physical dimensions of the type-A SIDGS cell. Note that coupling coefficients k_{ij} and Q can be derived as

$$k_{ij} = \text{FBW} \times M_{ij} \tag{17}$$

$$Q_i = \frac{1}{\text{FBW} \times M_{\text{Si}}^2}. \tag{18}$$

Thus, the corresponding main coupling coefficients and external quality factor can be obtained from the investigation mentioned earlier. With proper dimensions of the type-A SIDGS cells and optimized coupling relationships, the single-band SIDGS BPF is designed. The theoretical S-parameters calculated by coupling matrix and the lossless simulation result are shown in Fig. 16, which exhibits a fairly fine agreement. Then, a single-band BPF is fabricated, as shown in Fig. 17. Besides, radiation/conductor/dielectric loss rates of the BPF are simulated and calculated, as shown in Fig. 18. The radiation loss is simulated under the case of lossless metal and substrate (i.e., S_{11r}, S_{21r}). The radiation loss L_r is calculated as

$$L_r = 1 - |S_{11r}|^2 - |S_{21r}|^2. \tag{19}$$

The conductor loss L_c and dielectric loss L_d can be calculated under the cases of lossless dielectric (i.e., S_{11c} and S_{21c}) or

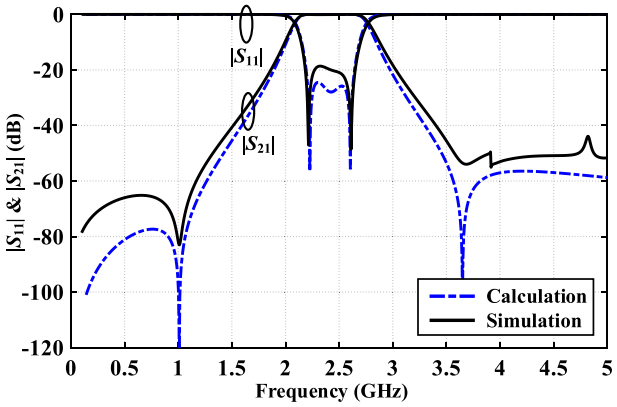

Fig. 16. Lossless simulated and synthesized $|S_{11}|$ and $|S_{21}|$ of the single-band BPF.

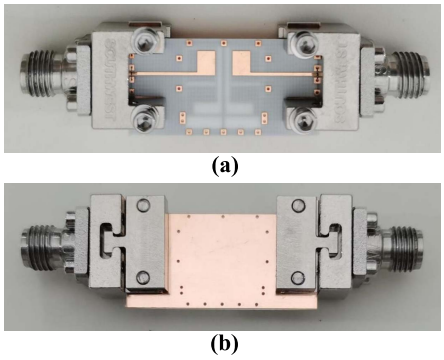

Fig. 17. Photograph of the proposed single-band BPF. (a) Top view. (b) Bottom view. $l_{11} = 4.6$, $l_{12} = 4.11$, $l_{13} = 3.75$, $l_{14} = 3.93$, $l_{15} = 3.15$, $d_{11} = 0.2$, $d_{12} = 0.2$, $d_{13} = 0.15$, $d_{14} = 0.17$, $d_{15} = 0.17$, $w_{11} = 0.17$, $w_{12} = 0.1$, $w_{13} = 2.25$, $w_{14} = 0.22$, $w_{15} = 0.1$, $w_{16} = 0.5$, $s_{11} = 6.9$, $s_{12} = 5.07$, $s_{13} = 7.52$, $s_{14} = 1.55$, $s_{15} = 1.7$, $s_{16} = 4.49$, $w_{t1} = 2.4$, and $l_{t1} = 3.28$, unit: mm.

lossless metal (i.e., S_{11d} and S_{21d}), respectively. L_c and L_d can be derived as

$$L_{c,d} = 1 - |S_{11c,d}|^2 - |S_{21c,d}|^2 - L_r. \tag{20}$$

The calculated radiation loss under the case of lossless substrate and metal is less than 13% up to 20 GHz.

The simulated and measured results of S-parameters are shown in Fig. 19. The Agilent 5230A network analyzer is used to measure. The center frequency of the BPF is 2.4 GHz with the 3-dB FBW of 24%. The minimum in-band insertion loss is 1.62 dB. Meanwhile, the stopband is up to 19.7 GHz with a rejection level higher than 31 dB. The measured stopband total loss is less than 30% up to 19 GHz except a high loss point at 14.1 GHz, as shown in Fig. 18. The simulated loss is solved under the case of the complete filter structure without the connectors. Note that the radiation at 14.1 GHz (i.e., green dashed line) in Fig. 18 is mainly allocated at the feed line surrounded by the metal-vias at the side of the filter. Meanwhile, with the implementation of connectors for test, the feed line is longer, while the EM fields of the ground at the side are affected. Thus, the radiation around 14.1 GHz (i.e., black solid line) in measurement further

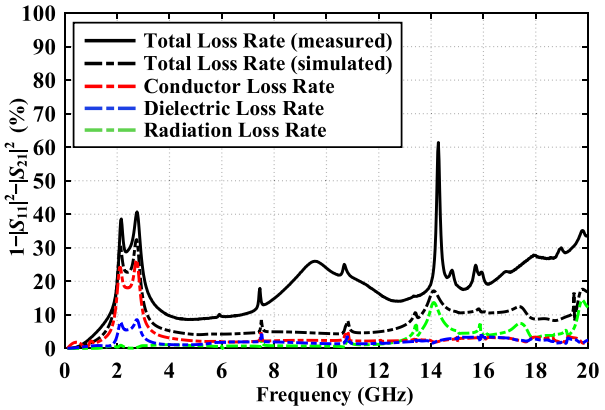

Fig. 18. Measured/simulated total loss rates and calculated radiation/conductor/dielectric loss rates of the single-band BPF.

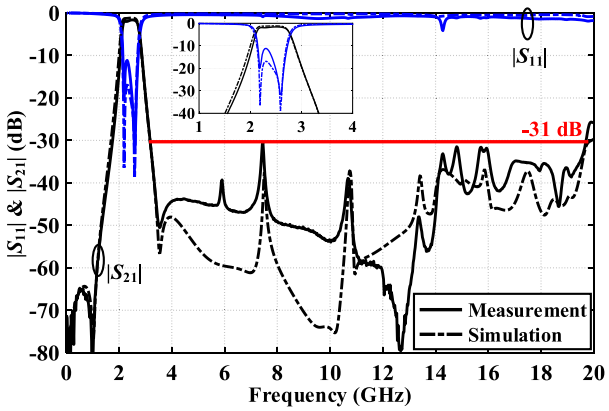

Fig. 19. Measured and simulated results of the proposed single-band BPF.

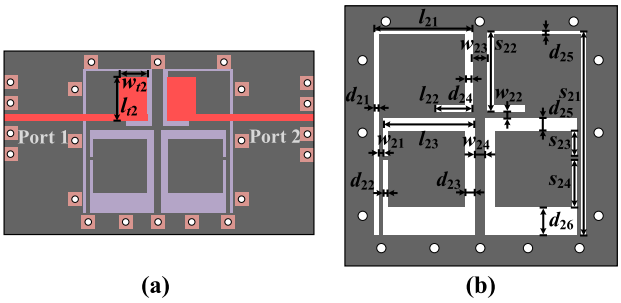

Fig. 20. Configuration of the dual-band BPF. (a) Top view. (b) Details of the middle layer.

increases. In addition, the core circuit size of the BPF is 12.3 mm × 12.2 mm (i.e., 0.16 λ_g × 0.16 λ_g, where λ_g is the microstrip guided wavelength at the center frequency of 2.4 GHz). Note that the feed line is shorter compared to the previous work [26], which improves the performance. A comparison of the single-band filter with the state of the arts is shown in Table I, which reveals that the proposed filter has merits of wide upper stopband, low radiation loss, and compact size.

TABLE I
COMPARISON OF STATE-OF-THE-ART SINGLE-BAND FILTERS

Ref.	[8]	[18]	[19]	[20]	[24]	**This Work**
Technology	SIW	Microstrip	Microstrip	Microstrip	DGS	**SIDGS**
f_0 (GHz)	4.83	0.9	2.45	1.5	2.48	**2.4**
IL* (dB)	1.2	1.7	3.0	2.52	1.08	**1.62**
FBW (%)	1.4	21	6.0	8.9	10.8	**24.6**
Stopband Rejection	>15 dB up to $1.3f_0$	>40 dB up to $7.4f_0$	>30 dB up to $5.3f_0$	>23.7 dB up to $10.6f_0$	>30 dB up to $12f_0$	**>31 dB up to $8.2f_0$**
Radiation Loss$^{\Delta}$	Low	N/A	Low	High	Medium 30% at 14 GHz	**Low <13% up to 20 GHz**
Total Loss$^{\diamond}$(<30%)	Up to 6.1 GHz$^{\diamond\diamond}$ ($1.4f_0$)	N/A	Up to 13.8 GHz$^{\diamond\diamond}$ ($5.6f_0$)	Up to 4 GHz$^{\diamond\diamond}$ ($2.7f_0$)	Up to 14 GHz$^{\diamond\diamond}$ ($5.6f_0$)	**Up to 19.3 GHz$^{\diamond\diamond\diamond}$ ($8f_0$)**
Unloaded Q	228	120	N/A	N/A	N/A	**99/101**
Core Circuit Size	1000 mm^2	46 mm^2	90 mm^2	0.0192 (λ_g^2) 777 mm^2	0.1122 (λ_g^2) 847 mm^2	**0.0256 (λ_g^2) 150 mm^2**

*: Insertion loss. $^{\Delta}$: Calculated radiation loss under case of lossless substrate and metal.
$^{\diamond}$: Measured stopband total loss including radiation, metal, and substrate loss. $^{\diamond\diamond}$: Estimated from the paper. $^{\diamond\diamond\diamond}$: Except a high loss point at 14.1 GHz.

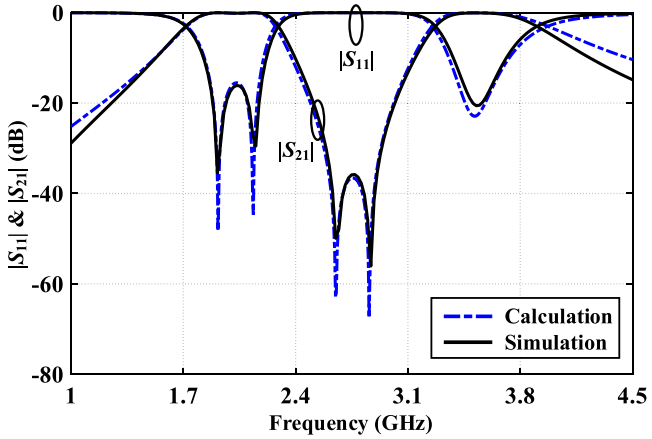

Fig. 21. Lossless simulated and synthesized $|S_{11}|$ and $|S_{21}|$ of the dual-band BPF.

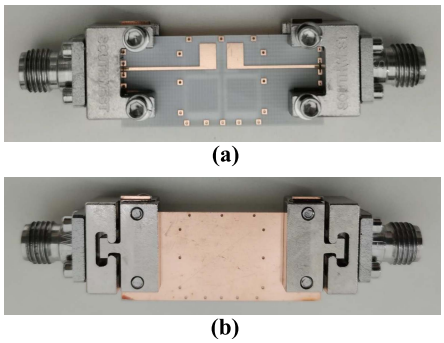

Fig. 22. Photograph of the proposed dual-band BPF. (a) Top view. (b) Bottom view. $l_{21} = 5.1$, $l_{22} = 2$, $l_{23} = 4.9$, $d_{21} = 0.2$, $d_{22} = 0.2$, $d_{23} = 0.35$, $d_{24} = 0.4$, $d_{25} = 0.5$, $d_{26} = 1.2$, $w_{21} = 0.1$, $w_{22} = 0.32$, $w_{23} = 0.7$, $w_{24} = 0.5$, $s_{21} = 11$, $s_{22} = 4.3$, $s_{23} = 2.1$, $s_{24} = 2.38$, $w_{t2} = 2.5$, and $l_{t2} = 3.68$, unit: mm.

B. Dual-Band BPF Design

A prototype of a two-order dual-band BPF is proposed based on the type-B SIDGS cell, as shown in Fig. 20. Then, the BPF is implemented with specifications as follows: lower center frequency of 2.0 GHz, 3-dB FBW = 26.0%, 15-dB return loss and upper center frequency of 3.55 GHz, 3-dB FBW = 15.4%, and 15-dB return loss. The optimized coupling matrix $[M_p]$ can be exhibited as follows [36]:

$$\begin{pmatrix} 0 & 0.6533 & 0.0201 & 0 & 0 & 0 \\ 0.6533 & 0 & 0.7090 & 0.0401 & 0.4598 & 0 \\ 0.0201 & 0.7090 & 0 & -0.0050 & 0.0401 & 0 \\ 0 & 0.0401 & -0.0050 & 0 & 0.7090 & 0.0201 \\ 0 & 0.4598 & 0.0401 & 0.7090 & 0 & 0.6533 \\ 0 & 0 & 0 & 0.0201 & 0.6533 & 0 \end{pmatrix}. \quad (21)$$

Here, the center frequencies are determined by the physical dimensions of the type-B SIDGS cell. The theoretical *S*-parameters calculated by the coupling matrix and the lossless simulation result are shown in Fig. 21. Then, a dual-band BPF is fabricated, as shown in Fig. 22. Besides, radiation/conductor/dielectric loss rates of the BPF are simulated and calculated, as shown in Fig. 23. The calculated radiation loss under the case of lossless substrate and metal is less than 12% up to 16.7 GHz.

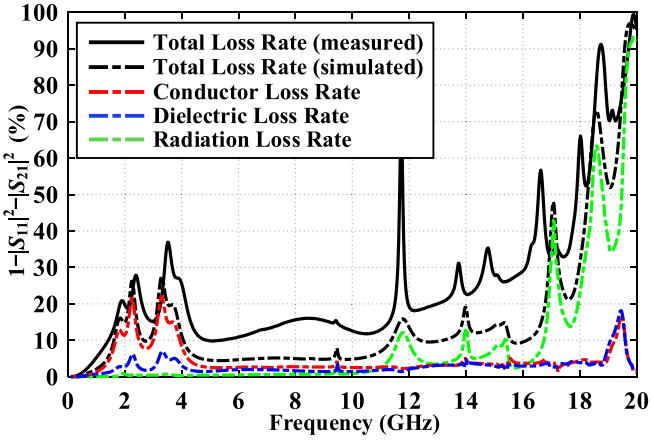

Fig. 23. Measured/simulated total loss rates and calculated radiation/conductor/dielectric loss rates of the dual-band BPF.

The simulated and measured results of S-parameters are shown in Fig. 24. The center frequency of lower passband is 2.1 GHz with 3-dB FBW of 25.2% and the minimum in-band insertion loss of 0.95 dB. The center frequency of upper passband is 3.78 GHz with 3-dB FBW of 12.7% and

TABLE II
COMPARISON OF STATE-OF-THE-ART DUAL-BAND FILTERS

Ref.	[9]	[14]	[21]	[22]	[25]	**This Work**
Technology	SIW	CPW to microstrip	Microstrip	Microstrip	DGS	**SIDGS**
f_1/f_2 (GHz)	2.4/5.0	1.53/2.16	2.4/5.2	2.4/6	3.16/3.90	**2.10/3.78**
IL* (dB)	1.47/1.01	0.8/1.8	2.27/2.88	1.85/2.98	1.87/1.67	**0.95/1.39**
FBW (%)	1/1	10.6/3.6	10.6/6	5/4.7	8.5/7.2	**25.2/12.7**
Stopband Rejection	N/A	N/A	>32.2 dB up to $3.75f_1$	>30 dB up to $8.3f_1$	>30 dB up to $12.6f_1$	**>23 dB up to $8.5f_1$**
Radiation Loss$^{\Delta}$	Low	N/A	High	High	High	**Low <12% up to 16.7 GHz**
Total Loss$^{\diamond}$(<16%)	N/A	N/A	Up to 5.7 GHz$^{\diamond\diamond}$ ($2.4f_1$)	Up to 8.3 GHz$^{\diamond\diamond}$ ($3.5f_1$)	Up to 11 GHz$^{\diamond\diamond}$ ($3.5f_1$)	**Up to 11.5 GHz ($5.5f_1$)**
Unloaded Q	>1000	108/137	N/A	N/A	N/A	**95/129**
Core Circuit Size	6451 mm^2	0.0625 (λ_g^2)	N/A	N/A	0.0820 (λ_g^2) 263 mm^2	**0.0169 (λ_g^2) 150 mm^2**

*: Insertion loss. $^{\Delta}$: Calculated radiation loss under case of lossless substrate and metal.
$^{\diamond}$: Measured stopband total loss including radiation, metal, and substrate loss. $^{\diamond\diamond}$: Estimated from the paper.

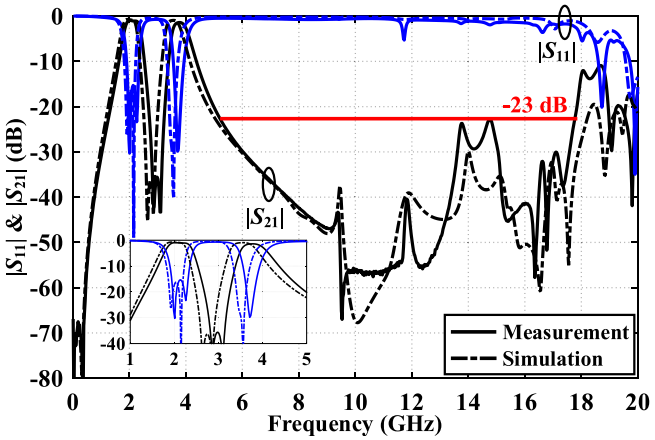

Fig. 24. Measured and simulated results of the proposed dual-band BPF.

the minimum in-band insertion loss of 1.39 dB. Moreover, the stopband with a rejection level higher than 23 dB is up to 17.8 GHz. Furthermore, Fig. 23 shows that the measured stopband total loss is less than 16% up to 11.5 GHz. The operation of the radiation at 11.8 GHz in Fig. 23 is similar to the effect of 14.1 GHz in Fig. 18. The core circuit size of the BPF is 12.3 mm × 12.2 mm (i.e., 0.13 λ_g × 0.13 λ_g, where λ_g is the microstrip guided wavelength at the lower passband center frequency of 2.1 GHz). The difference between the measured and simulated results is mainly caused by the fabrication errors. A comparison of the dual-band filter with the state of the arts is shown in Table II. It reveals that this filter has merits of wide upper stopband, low radiation loss, compact size, and low insertion loss.

V. CONCLUSION

In this article, two types of SIDGS resonant cells with different transmission responses are proposed. Both cells can not only introduce an ultrawide stopband bandwidth due to the strong slow-wave effect but also suppress their radiation loss in a wide range by their instinct structural superiority. Based on the proposed SIDGS resonant cells, single- and dual-band BPFs are analyzed, designed, and fabricated. The design examples inherit the merits of DGS, such as wide stopband, low insertion loss, and compact size. Meanwhile, a strong suppression of the radiation is also obtained. With such good performance and the instinct structure advantage of the flexible integration, the proposed SIDGS and single-/dual-band BPFs are attractive for practical applications.

APPENDIX

As shown in Figs. 3 and 5, the input impedances Z_A, Z_B, Z_C, and Z_D of the equivalent circuits can be calculated using the transmission line impedance equations [35], which can be

$$Z_A = Z_{12}\cdot\frac{Z_{13}(Z_X + jZ_{13}\tan\theta_{13}) + jZ_{12}\tan\theta_{12}(Z_{13} + jZ_X\tan\theta_{13})}{Z_{12}(Z_{13} + jZ_X\tan\theta_{13}) + jZ_{13}\tan\theta_{12}(Z_X + jZ_{13}\tan\theta_{13})} \tag{22}$$

$$Z_B = \frac{Z_{24}}{j}\cdot\frac{Z_{25}(Z_{26} - Z_{25}\tan\theta_{25}\tan\theta_{26}) - Z_{24}\tan\theta_{24}(Z_{25}\tan\theta_{26} + Z_{26}\tan\theta_{25})}{Z_{24}(Z_{25}\tan\theta_{26} + Z_{26}\tan\theta_{25}) + Z_{25}(Z_{26} - Z_{25}\tan\theta_{25}\tan\theta_{26})} \tag{23}$$

$$Z_C = \frac{Z_{34}}{j}\cdot\frac{Z_{35}(Z_{36} - Z_{35}\tan\theta_{35}\tan\theta_{36}) - Z_{34}\tan\theta_{34}(Z_{35}\tan\theta_{36} + Z_{36}\tan\theta_{35})}{Z_{34}(Z_{35}\tan\theta_{36} + Z_{36}\tan\theta_{35}) + Z_{35}(Z_{36} - Z_{35}\tan\theta_{35}\tan\theta_{36})} \tag{24}$$

$$Z_D = \frac{Z_{44}}{j}\cdot\frac{Z_{45}(Z_{46} - Z_{45}\tan\theta_{45}\tan\theta_{46}) - Z_{44}\tan\theta_{44}(Z_{45}\tan\theta_{46} + Z_{46}\tan\theta_{45})}{Z_{44}(Z_{45}\tan\theta_{46} + Z_{46}\tan\theta_{45}) + Z_{45}(Z_{46} - Z_{45}\tan\theta_{45}\tan\theta_{46})} \tag{25}$$

$$Z_X = \frac{Z_{14}}{j}\cdot\frac{Z_{15}(Z_{16} - Z_{15}\tan\theta_{15}\tan\theta_{16}) - Z_{14}\tan\theta_{14}(Z_{15}\tan\theta_{16} + Z_{16}\tan\theta_{15})}{Z_{14}(Z_{15}\tan\theta_{16} + Z_{16}\tan\theta_{15}) + Z_{15}(Z_{16} - Z_{15}\tan\theta_{15}\tan\theta_{16})} \tag{26}$$

expressed as (22)–(25), shown at the bottom of the previous page, where Z_X is expressed as (26).

ACKNOWLEDGMENT

The authors would like to thank Jie Zhou, Bingzheng Yang, Yunbo Rao, and Yiyang Shu for the technical discussions.

REFERENCES

[1] B. Archambeault, C. Brench, and S. Connor, "Review of printed-circuit-board level EMI/EMC issues and tools," *IEEE Trans. Electromagn. Compat.*, vol. 52, no. 2, pp. 455–461, May 2010.

[2] J. A. G. Malherbe, "Wideband bandpass filter with extremely wide upper stopband," *IEEE Trans. Microw. Theory Techn.*, vol. 66, no. 6, pp. 2822–2827, Jun. 2018.

[3] M. Brandolini, P. Rossi, D. Manstretta, and F. Svelto, "Toward multi-standard mobile terminals–fully integrated receivers requirements and architectures," *IEEE Trans. Microw. Theory Techn.*, vol. 53, no. 3, pp. 1026–1038, Mar. 2005.

[4] K. S. Yang, S. Pinel, I. K. Kim, and J. Laskar, "Low-loss integrated-waveguide passive circuits using liquid-crystal polymer system-on-package (SOP) technology for millimeter-wave applications," *IEEE Trans. Microw. Theory Techn.*, vol. 54, no. 12, pp. 4572–4579, Dec. 2006.

[5] A. Belenguer, A. L. Borja, H. Esteban, and V. E. Boria, "High-performance coplanar waveguide to empty substrate integrated coaxial line transition," *IEEE Trans. Microw. Theory Techn.*, vol. 63, no. 12, pp. 4027–4034, Dec. 2015.

[6] Z.-C. Hao, W. Hong, J.-X. Chen, X.-P. Chen, and K. Wu, "Compact super-wide bandpass substrate integrated waveguide (SIW) filters," *IEEE Trans. Microw. Theory Techn.*, vol. 53, no. 9, pp. 2968–2977, Sep. 2005.

[7] C. J. You, Z. N. Chen, X. W. Zhu, and K. Gong, "Single-layered SIW post-loaded electric coupling-enhanced structure and its filter applications," *IEEE Trans. Microw. Theory Techn.*, vol. 61, no. 1, pp. 125–130, Jan. 2013.

[8] L. Silvestri, A. Ghiotto, C. Tomassoni, M. Bozzi, and L. Perregrini, "Partially air-filled substrate integrated waveguide filters with full control of transmission zeros," *IEEE Trans. Microw. Theory Techn.*, vol. 67, no. 9, pp. 3673–3682, Sep. 2019.

[9] X. Liu, L. P. B. Katehi, and D. Peroulis, "Novel dual-band microwave filter using dual-capacitively-loaded cavity resonators," *IEEE Microw. Wireless Compon. Lett.*, vol. 20, no. 11, pp. 610–612, Nov. 2010.

[10] T. Lopetegi *et al.*, "New microstrip 'wiggly-line' filters with spurious passband suppression," *IEEE Trans. Microw. Theory Techn.*, vol. 49, no. 9, pp. 1593–1598, Sep. 2001.

[11] K. M. Shum, T. T. Mo, Q. Xue, and C. H. Chan, "A compact bandpass filter with two tuning transmission zeros using a CMRC resonator," *IEEE Trans. Microw. Theory Techn.*, vol. 53, no. 3, pp. 895–900, Mar. 2005.

[12] P. Cheong, S.-W. Fok, and K.-W. Tam, "Miniaturized parallel coupled-line bandpass filter with spurious-response suppression," *IEEE Trans. Microw. Theory Techn.*, vol. 53, no. 5, pp. 1810–1816, May 2005.

[13] S. Sun and L. Zhu, "Periodically nonuniform coupled microstrip-line filters with harmonic suppression using transmission zero reallocation," *IEEE Trans. Microw. Theory Techn.*, vol. 53, no. 5, pp. 1817–1822, May 2005.

[14] X. Yin Zhang and Q. Xue, "Novel dual-mode dual-band filters using coplanar-waveguide-fed ring resonators," *IEEE Trans. Microw. Theory Techn.*, vol. 55, no. 10, pp. 2183–2190, Oct. 2007.

[15] C.-H. Tseng and H.-Y. Shao, "A new dual-band microstrip bandpass filter using net-type resonators," *IEEE Microw. Wireless Compon. Lett.*, vol. 20, no. 4, pp. 196–198, Apr. 2010.

[16] J.-T. Kuo and E. Shih, "Microstrip stepped impedance resonator bandpass filter with an extended optimal rejection bandwidth," *IEEE Trans. Microw. Theory Techn.*, vol. 51, no. 5, pp. 1554–1559, May 2003.

[17] J. Garcia-Garcia *et al.*, "Spurious passband suppression in microstrip coupled line band pass filters by means of split ring resonators," *IEEE Microw. Wireless Compon. Lett.*, vol. 14, no. 9, pp. 416–418, Sep. 2004.

[18] B. A. Belyaev, A. M. Serzhantov, A. A. Leksikov, Y. F. Bal'va, and A. A. Leksikov, "Novel high-quality compact microstrip resonator and its application to bandpass filter," *IEEE Microw. Wireless Compon. Lett.*, vol. 25, no. 9, pp. 579–581, Sep. 2015.

[19] C.-L. Hsu and J.-T. Kuo, "A two-stage SIR bandpass filter with an ultra-wide upper rejection band," *IEEE Microw. Wireless Compon. Lett.*, vol. 17, no. 1, pp. 34–36, Jan. 2007.

[20] C. H. Kim and K. Chang, "Wide-stopband bandpass filters using asymmetric stepped-impedance resonators," *IEEE Microw. Wireless Compon. Lett.*, vol. 23, no. 2, pp. 69–71, Feb. 2013.

[21] C. H. Kim and K. Chang, "Independently controllable dual-band bandpass filters using asymmetric stepped-impedance resonators," *IEEE Trans. Microw. Theory Techn.*, vol. 59, no. 12, pp. 3037–3047, Dec. 2011.

[22] J.-T. Kuo and H.-P. Lin, "Dual-band bandpass filter with improved performance in extended upper rejection band," *IEEE Trans. Microw. Theory Techn.*, vol. 57, no. 4, pp. 824–829, Apr. 2009.

[23] A. Balalem, A. R. Ali, J. Machac, and A. Omar, "Quasi-elliptic microstrip low-pass filters using an interdigital DGS slot," *IEEE Microw. Wireless Compon. Lett.*, vol. 17, no. 8, pp. 586–588, Aug. 2007.

[24] X. Luo, J.-G. Ma, E.-P. Li, and K. Ma, "Hybrid microstrip T-stub/defected ground structure cell for electromagnetic interference bandpass filter design," *IEEE Trans. Electromagn. Compat.*, vol. 53, no. 3, pp. 717–725, Aug. 2011.

[25] Y. Rao, H. J. Qian, B. Yang, R. Gomez-Garcia, and X. Luo, "Dual-band bandpass filter and filtering power divider with ultra-wide upper stopband using hybrid microstrip/DGS dual-resonance cells," *IEEE Access*, vol. 8, pp. 23624–23637, 2020.

[26] D. Tang, C. Han, Z. Deng, H. J. Qian, and X. Luo, "Compact bandpass filter with wide stopband and low radiation loss using substrate integrated defected ground structure," in *IEEE MTT-S Int. Microw. Symp. Dig.*, Aug. 2020, pp. 1–4.

[27] R. Garg, I. Bahl, and M. Bozzi, *Microstrip Lines and Slotlines*, 3rd ed. Norwood, MA, USA: Artech House, 2013.

[28] D. Ahn, J. S. Park, C. S. Kim, J. Kim, Y. Qian, and T. Itoh, "A design of the low-pass filter using the novel microstrip defected ground structure," *IEEE Trans. Microw. Theory Techn.*, vol. 49, no. 1, pp. 86–93, Jan. 2001.

[29] J.-S. Hong, *Microstrip Filters for RF/Microwave Applications*, 2nd ed. New York, NY, USA: Wiley, 2011.

[30] G. Macchiarella and S. Tamiazzo, "Design techniques for dual-passband filters," *IEEE Trans. Microw. Theory Techn.*, vol. 53, no. 11, pp. 3265–3271, Nov. 2005.

[31] P. Ma, B. Wei, J. Hong, X. Guo, B. Cao, and L. Jiang, "Coupling matrix compression technique for high-isolation dual-mode dual-band filters," *IEEE Trans. Microw. Theory Techn.*, vol. 66, no. 6, pp. 2814–2821, Jun. 2018.

[32] J.-S. Hong and M. J. Lancaster, "Theory and experiment of novel microstrip slow-wave open-loop resonator filters," *IEEE Trans. Microw. Theory Techn.*, vol. 45, no. 12, pp. 2358–2365, Dec. 1997.

[33] A. Ebrahimi, W. Withayachumnankul, S. F. Al-Sarawi, and D. Abbott, "Compact dual-mode wideband filter based on complementary split-ring resonator," *IEEE Microw. Wireless Compon. Lett.*, vol. 24, no. 3, pp. 152–154, Mar. 2014.

[34] H. Shigesawa, M. Tsjui, and A. A. Oliner, "Conductor-backed slot line and coplanar waveguide: Dangers and full-wave analyses," in *IEEE MTT-S Int. Microw. Symp. Dig.*, New York, NY, USA, Jun. 1988, pp. 199–202.

[35] D. M. Pozar, *Microwave Engineering*, 4th ed. New York, NY, USA: Wiley, 2012.

[36] X. Luo, B. Yang, and H. J. Qian, "Adaptive synthesis for resonator-coupled filters based on particle swarm optimization," *IEEE Trans. Microw. Theory Techn.*, vol. 67, no. 2, pp. 712–725, Feb. 2019.

[37] Y.-S. Lin, W.-C. Ku, C.-H. Wang, and C. H. Chen, "Wideband coplanar waveguide bandpass filters with good stopband rejection," *IEEE Microw. Wireless Compon. Lett.*, vol. 14, no. 9, pp. 422–424, Sep. 2004.

[38] A. Velez, F. Aznar, J. Bonache, M. C. Velázquez-Ahumada, J. Martel, and F. Martín, "Open complementary split ring resonators (OCSRRs) and their application to wideband CPW band pass filters," *IEEE Microw. Wireless Compon. Lett.*, vol. 19, no. 4, pp. 197–199, Apr. 2009.

[39] T. B. Lim and L. Zhu, "Highly selective differential-mode wideband bandpass filter for UWB application," *IEEE Microw. Wireless Compon. Lett.*, vol. 21, no. 3, pp. 133–135, Mar. 2011.

[40] X. Luo, J.-G. Ma, and E.-P. Li, "Wideband bandpass filter with wide stopband using loaded BCMC stub and short-stub," *IEEE Microw. Wireless Compon. Lett.*, vol. 21, no. 7, pp. 353–355, Jul. 2011.

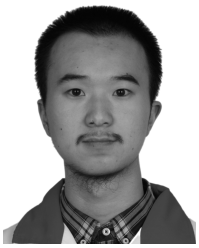

Deshan Tang (Student Member, IEEE) is currently pursuing the B.E. degree in information and communication engineering at the University of Electronic Science and Technology of China, Chengdu, China.

His research interests include the reconfigurable RF/microwave filter and passive components.

Mr. Tang was a recipient of the IEEE IMS Best Student Paper Award Finalist in 2020 and the IEEE IMS Advanced Practice Paper Award Finalist in 2020.

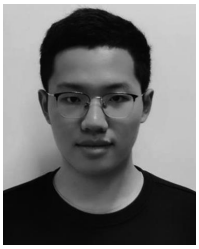

Changxuan Han (Student Member, IEEE) is currently pursuing the B.E. degree in electronic science and technology at the University of Electronic Science and Technology of China, Chengdu, China.

His research interests include the integrated microwave/millimeter-wave receiver and multifunction passive components.

Mr. Han was a recipient of the IEEE IMS Student Design Competition Award in 2019 and the IEEE RFIT Best Student Paper Award in 2019.

Zhixian Deng (Graduate Student Member, IEEE) received the B.E. degree in microelectronics science and engineering from the University of Electronic Science and Technology of China, Chengdu, China, in 2019, where he is currently pursuing the Ph.D. degree in electronic science and technology.

His research interests include the reconfigurable microwave/millimeter-wave transceiver and passive components, especially integrated circuits.

Mr. Deng was a recipient of the IEEE IMS Student Design Competition Awards from 2017 to 2019.

Huizhen Jenny Qian (Member, IEEE) received the B.E., master's, and Ph.D. degrees in electronic engineering from the University of Electronic Science and Technology of China (UESTC), Chengdu, China, in 2008, 2011, and 2018, respectively.

Since 2019, she has been a Faculty Member with the Center for Integrated Circuits, UESTC, where she is currently an Associate Professor. In 2020, she was appointed as the Vice-Director of the Center for Advanced Semiconductor and Integrated Micro-System, UESTC. Her research interests include the wideband microwave/millimeter-wave transceiver, reconfigurable passive circuits, and on-chip array systems.

Dr. Qian was a recipient/co-recipient of the 2018 IEEE MTT-Society Graduate Fellowship Award, the IEEE IWS Best Student Paper Awards in 2015 and 2018, the IEEE IMS Student Design Competition Awards in 2017 and 2018, and the IEEE RFIT Best Student Paper Awards in 2016 and 2019.

Xun Luo (Senior Member, IEEE) received the B.E. and Ph.D. degrees in electronic engineering from the University of Electronic Science and Technology of China (UESTC), Chengdu, China, in 2005 and 2011, respectively.

From 2010 to 2013, he was the Project Manager with Huawei Technologies Company, Ltd., Shenzhen, China, to guide research and development projects of multiband microwave/millimeter-wave (mm-wave) integrated systems for backhaul and wireless communication. Before joining UESTC, he was an Assistant Professor with the Department of Microelectronics, Delft University of Technology, Delft, The Netherlands. Since 2015, he has been a Full Professor with UESTC, where he has been appointed as the Executive Director of the Center for Integrated Circuits. Since 2020, he has been the Head of the Center for Advanced Semiconductor and Integrated Micro-System, UESTC. He has authored or coauthored more than 100 journal articles and conference papers. He holds 32 patents. His research interests include the RF/microwave/mm-wave integrated circuits, multiple-resonance terahertz (THz) modules, multiband backhaul/wireless systems, reconfigurable passive circuits, smart antenna, and system in package.

Dr. Luo is also a Technical Program Committee Member of the IEEE International Microwave Symposium (IMS), the IEEE Radio Frequency Integrated Circuits Symposium (RFIC), and the IEEE International Wireless Symposium (IWS). He is also a Technical Committee Member of the MTT-4 on Microwave Passive Components and Transmission Line Structures, the MTT-5 on Filters, and the MTT-23 on Wireless Communications. He was bestowed by China as the China Overseas Chinese Contribution Award in 2016. He received the UESTC Distinguished Innovation and Teaching Award in 2018 and the UESTC Outstanding Undergraduate Teaching Promotion Award in 2016. His research group BEAM X-Lab received multiple best paper awards and best design competition awards, including the IEEE IWS Best Student Paper Awards in 2015 and 2018, the IEEE IMS Best Student Design Competition Awards from 2017 to 2019, the IEEE IMS Sixty-Second Presentation Competition Award in 2019, and multiple best paper award finalists at the IEEE conferences. He is also the Vice-Chair of the IEEE MTT-Society Chengdu Chapter. He is also the TPC Co-Chair of the IEEE IWS in 2018 and the IEEE RFIT in 2019. He also serves as a Track Editor for the IEEE MICROWAVE AND WIRELESS COMPONENTS LETTERS and an Associate Editor for the *IET Microwaves, Antennas & Propagation*.